Applied Computing and Geosciences 13 (2022) 100079

Contents lists available at ScienceDirect

Applied Computing and Geosciences

journal homepage: www.sciencedirect.com/journal/applied-computing-and-geosciences

A model of fluid expulsion from compacting tight sedimentary rocks based on the Toggle-Switch algorithm

Magnus Wangen

Institute for Energy Technology, P.O.Box 40, 2027, Kjeller, Norway

ARTICLE INFO

Keywords:
Fluid expulsion
Compaction
Burial
Porosity

ABSTRACT

Expulsion of fluids from tight rocks is an important process in sedimentary basins for phenomena such as distribution of overpressure and primary migration of hydrocarbons. This paper shows that the "Toggle Switch" (TS) algorithm of Miller and Nur is well-suited to model expulsion of brine by hydraulic fracturing from tight rocks undergoing compaction. Local random overpressure is generated in the TS algorithm using a void ratio function with random compaction length. The TS algorithm equilibrates critical fluid pressure by local exchange of excess fluid. We show that the algorithm gives net migration of fluid upwards, because the least compressive stress is decreasing towards the surface. The random void ratio makes the total expulsion rate from the layer intermittent. In the limit of zero cell size the expulsion rate approaches a mean value. When the rock has a random strength, it is shown that critically pressured clusters remain after the TS algorithm has been applied. The implementation of the algorithm is mass conservative, which ensures that the expelled mass is exactly the mass of pore fluid lost by compaction. Expressions are derived for the rate of fluid expulsion and for an effective fracture permeability.

1. Introduction

High overpressure is commonly encountered in sedimentary basins (Osborne and Swarbrick, 1997; Darby et al., 1998; Nordgård Bolås et al., 2004). In the Central North Sea, high overpressure is found in Jurassic and Triassic reservoirs at depths below 2 km–3 km (Yardley and Nwozor, 2017). Rapid deposition of low-permeable sediment is a known process for overpressure generation (Gibson, 1958; Bethke and Corbet, 1988; Audet and Fowler, 1992; Wangen, 1992, 1997, 2001). The increasing weight and temperature during deposition and burial lead to compaction of the pore space. A low permeability makes the expulsion of pore fluids difficult at the same pace as porosity reduction, which leads to the build-up of a large overpressure gradient. Overpressure is here understood to be the fluid pressure minus the hydrostatic pressure. The hydrostatic pressure is the weight of the water column up to the sediment surface. A large vertical overpressure gradient implies a rapidly increasing overpressure with depth.

Expulsion driven by hydraulic fracturing could be the reason why fluid pressures are rarely observed above the overburden pressure in sedimentary basins. Hydraulic fracturing takes place when the fluid pressure exceeds the least compressive stress, and the resulting fractures become vertical if the least compressive stress is horizontal (Hubbert and Willis, 1957). In basin modelling, there are few models for expulsion driven by hydraulic fracturing in low-permeable units undergoing compaction, which at the same time limit the pressure build-up.

The compaction of sediments can be mechanical and chemical (Bjørlykke and Høeg, 1997). When the sediments are undercompacted, the process is referred to as disequilibrium compaction (Osborne and Swarbrick, 1997). Purely mechanical clay compaction is controlled by the effective pressure, which is the difference between the overburden (lithostatic pressure) and the fluid pressure (Atkinson and Bransby, 1978; Whitlow, 2001; Nordgård Bolås et al., 2004). Mechanical compaction stops when fluid pressure approaches the lithostatic pressure, and the effective pressure approaches zero. Young and unlithified shallow sediments compact mechanically, while deeper lithified sediments at temperatures above 70 °C compact chemically (Nordgård Bolås et al., 2004; Bjørlykke and Høeg, 1997). Chemical compaction and cementation of the pore space are largely independent of fluid pressure (Bjørlykke and Høeg, 1997; Walderhaug et al., 2001). Therefore, chemical porosity reduction is not retarded by pressure build-up and it could, unless limited by hydraulic fracturing, go beyond the least compressive stress. Besides, hydrocarbon generation and smectite dehydration are thermally controlled chemical processes generating fluids and overpressure (Bjørlykke, 2010; Tremosa et al., 2020).

E-mail address: Magnus.Wangen@ife.no.

https://doi.org/10.1016/j.acags.2022.100079
Received 4 July 2021; Received in revised form 21 January 2022; Accepted 21 January 2022
Available online 24 January 2022
2590-1974/© 2022 The Author. Published by Elsevier Ltd. This is an open access article under the CC BY license (http://creativecommons.org/licenses/by/4.0/).

A number of studies (Teige et al., 1999; Hermanrud et al., 1998; Nordgård Bolås et al., 2004; Hermanrud et al., 2005) of compaction and overpressure in shale units concluded that porosity reduction is caused by stress insensitive processes. Wells with high overpressure did not have higher shale porosities than wells with little or no overpressure. Hermanrud and Undertun (2019) point out that it is difficult to measure overpressure in shale because of the low permeability, and that well logging methods relying on relationships between porosity measurements and overpressure should be used with care.

There are a large number of approaches to the modelling of hydraulic fracturing induced by fluid injection by wells. Examples are the classical models of one hydraulic fracture (Perkins and Kern, 1961; Nordgren, 1972; Charlez, 1997), models of discrete fractures such as the beam model (Tzschichholz et al., 1994; Tzschichholz and Herrmann, 1995; Tzschichholz and Wangen, 1998; Wangen, 2011), discrete element models (Bruel, 2007; Bruel and Charlety, 2007; Riahi and Damjanac, 2013; Itasca International, 2016), and models populated with discrete fractures that may be activated (Izadi and Elsworth, 2014; Verdon et al., 2015). Other models of hydraulic fracturing do not take into account each fracture but account for a fracture network using fracture permeability (Wangen, 2019).

There are models of natural hydraulic fracturing, where the fracturing is driven by fluid pressure imposed on the boundary of a layer (Sachau et al., 2015; de Riese et al., 2020), by an internal fluid source representing hydrocarbon generation (Panahi et al., 2019) or by internal reaction-induced fracturing (Hafver et al., 2014; Zhang et al., 2019). The concept of porosity waves has been introduced as a model of fluid transport through nearly impermeable layers (Appold and Nunn, 2002; Yarushina and Podladchikov, 2015; Yarushina et al., 2015). The driving force behind porosity waves is buoyancy and they ascend by viscous deformations of the sedimentary matrix.

Only a few experiments have studied hydraulic fracturing from an internal source. Kobchenko et al. (2011, 2014) used a Hele-Shaw cell to study the nucleation, propagation, and coalescence of fractures within an elastic medium of gelatin due to CO_2 production from the fermentation of sugar. They quantified how a fracture network develops, and how the dynamics of opening and closing of fractures controls an intermittent fluid transport. Furthermore, release of gas was observed at a frequency that depended on the gas production rate, but not on the system size.

In this expulsion model, the hydraulic fracturing process builds on the "Toggle Switch" (TS) model of Miller and Nur (2000). They proposed a cellular automaton model for natural hydraulic fracturing driven by an internal fluid source in an impermeable horizontal 2-D rock unit. Since the rock is impermeable, there is no fluid flow or fluid redistribution in the TS model until the fluid pressure in a cell reaches the fracture limit. When a cell fractures, it exchanges excess fluid with its nearest neighbours. The exchange of fluid with the nearest neighbour cells might make one or more neighbour cells critical. This implementation is different from Miller and Nur (2000) in several ways. Firstly, Miller and Nur (2000) studied the initial and transient phase of pressure build-up until a sample spanning cluster of the critical cells appears. Very little fluid is expelled across the layer boundaries during this initial phase. Here, the model is for the quasi-stationary phase that follows the transient initial phase, which has a quasi-stationary expulsion rate. This quasi-stationary state lasts as long as the porosity reduction upholds a critical fluid pressure. Secondly, this implementation deals with fluid expulsion in a vertical cross-section where the critical fluid pressure increases with depth. The model of Miller and Nur (2000) considered pressure build-up and fracturing in a horizontal plane. A third difference is that this implementation has overpressure generation from compaction by porosity reduction. Miller and Nur (2000) based the overpressure generation on an assumed crustal strain rate. For instance, the proposed implementation could represent the expulsion of excess fluids out of a high-pressure and high-temperature sedimentary (HPHT) layer.

This paper is organized as follows. The TS cellular automaton is introduced as a model for fluid expulsion. The void ratio and the corresponding pressure build-up in impermeable rocks are introduced for use with the expulsion model. Then, the pressure equilibration by the TS algorithm is explained. Some examples of fluid expulsion by hydraulic fracturing are presented – first for cases without random rock strength before cases with random strength. An estimate of the expulsion rate is derived and tested on a case with random rock strength. The expulsion model is discussed in light of pressure observations in sedimentary basins.

2. A cellular automaton model for fluid expulsion

The TS algorithm is a cellular automaton model of local microfracturing and local redistribution of pore fluid (Miller and Nur, 2000). A fracture network is open during the local redistribution of fluids, but the model does not produce lasting fracture porosity or fracture permeability. A cellular automaton consists of a regular grid of cells and a rule that changes the state of the cells. In the TS model, the cells can be in two states – either a critical state, where the fluid pressure is larger than the least compressive stress, or otherwise a non-critical state.

Overpressure build-up is driven by deposition of sediments. The deposition process is discretized with steps, where a small thickness of sediment is deposited uniformly over the seabed at each step. The addition of a small thickness of sediment over the seabed leads to a small amount of compaction and thereby a small amount of pressure build-up. The implementation of Miller and Nur (2000) had overpressure generation from a generic source term in each cell, which was estimated from crustal strain rates. The pressure build-up may make some cells critical. The TS algorithm makes critical cells non-critical using an iterative procedure. An iteration step begins by listing all critical cells, and the listed cells are then fractured. The fracturing of a cell implies that the cell exchanges fluid with its four nearest neighbours, and the result is that all five cells (the critical cell and its four nearest neighbours) get the same overpressure. The fracturing step is the rule in a cellular automaton process that changes the state of the cells. The TS algorithm provides a simple representation of the fluid redistribution due to the complex microfracturing and re-fracturing in tight rock.

The condition for the fracturing of a cell is that the fluid pressure exceeds the least compressive stress with added random strength. The least compressive stress is taken to be horizontal and is a linear function of depth. Random strength can be added to each cell, which represents local variations in rock strength or local variations in the stress field. The strength is an effective cell property that serves as a threshold above the least compressive stress for microfracturing or re-fracturing of the cells to occur. It is for simplicity taken to be a static property. Therefore, the healing of the fractures is not accounted for.

Iteration over critical cells is repeated until there are no more critical cells. In the case of zero random strength, the fracturing algorithm always ends by making all cells non-critical. In the opposite case of non-zero random strength, there may remain patterns of critically pressured cells that have the same pressure as their neighbours. Fracturing these cell will not change anything because a new iteration produces the same pattern of critical cells. The procedure stops when a new iteration reproduces the same pattern of critical cells as the previous iteration.

3. A linear void ratio function

The porosity is a complicated and very heterogeneous property, which is here represented by a simple function of depth. The pores are assumed fully saturated with brine. The porosity loss and the compaction of a sediment layer is simulated assuming a linear relationship between the void ratio and the sediment depth from the basin surface:

$$e(\zeta) = e_0 \cdot \left(1 - \frac{(\zeta_T - \zeta)}{\zeta_c}\right), \tag{1}$$

where e_0 is the surface void ratio, ζ_c is the compaction length, ζ_T is the height of the sediment surface and ζ is a vertical position in the layer. Both ζ_T and ζ are measured as net (porosity free) rock from a reference position, $\zeta = 0$ (see Fig. 1). The difference $\zeta_T - \zeta$ is the sediment depth from the seabed measured as porosity free rock, and the compaction length ζ_c controls how steep the compaction is with the depth. Function (1) is a linear approximation of the void ratio for a layer during a time interval that is short compared with the full burial history of the layer. Therefore, the function (1) is not a good approximation for the entire burial history. The void ratio function (1) can be calibrated against compaction trends (Lee et al., 2020).

The porosity of sedimentary rocks is not a smooth function of depth, but a noisy function due to the heterogeneous nature of sediments (Josh et al., 2012). The void ratio, and thereby the porosity, is made random by means of a random compaction length ζ_c. The value of ζ_c must be much larger than $\zeta_T - \zeta$ for ζ-positions inside the layer, otherwise the void ratio becomes less than zero. The random compaction length is introduced as

$$\zeta_c = \zeta_{c,0} + \Delta\zeta_c \cdot r \tag{2}$$

where r is a uniformly distributed random variable between 0 and 1. The average void ratio for a constant ζ-position is

$$\overline{e}(\zeta) = \int_0^1 e(\zeta, r)\, dr = e_0 \cdot \left(1 - \frac{(\zeta_T - \zeta)}{\zeta_D}\right) \quad \text{where} \quad \zeta_D = \frac{\Delta\zeta_c}{\ln(1 + \Delta\zeta_c/\zeta_{c,0})}. \tag{3}$$

the average void ratio (3) has the same form as the linear void ratio function (1), but with a shorter compaction length, ζ_D. It is also useful to have the average void ratio for the entire shale layer:

$$\overline{\overline{e}} = \frac{1}{\zeta_2 - \zeta_1} \int_{\zeta_1}^{\zeta_2} \overline{e}(\zeta)\, d\zeta = \overline{e}(\zeta_m) \quad \text{where} \quad \zeta_m = \frac{1}{2}(\zeta_1 + \zeta_2) \tag{4}$$

and where the layer is in the range from $\zeta = \zeta_1$ to $\zeta = \zeta_2$ (see Fig. 1). The average $\overline{\overline{e}}$ is the same as the average void ratio at the layer centre position ζ_m. The compaction length ζ_D has the limit $\zeta_D \to \zeta_{c,0}$ when $\Delta\zeta_c \to 0$, and the average for the whole unit, $\overline{\overline{e}}$, has the limit $\overline{\overline{e}} \to e(\zeta_m)$ when $\Delta\zeta_c \to 0$. It is the void ratio at the centre, which is as expected for a linear void ratio function.

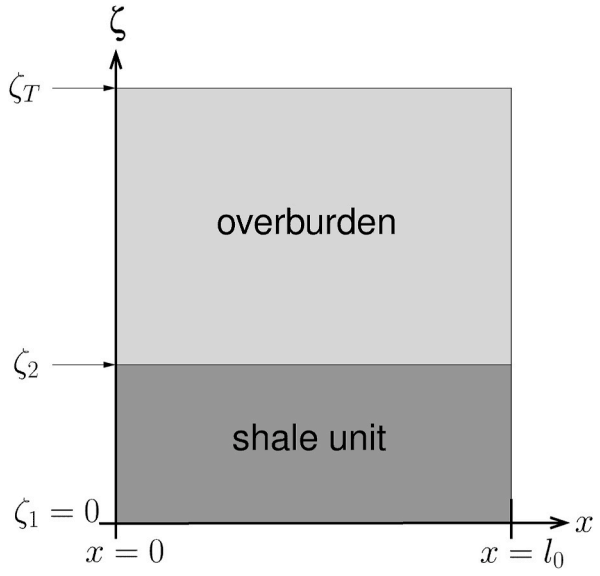

Fig. 1. The vertical ζ-axis points upwards. The shale layer is in the ζ-interval from $\zeta_1 = 0$ to ζ_2, and the basin surface is at $\zeta = \zeta_T$.

4. Local pressure build-up

Decreasing porosity during burial increases the overpressure. The rock is assumed impermeable and mass conservation is used to obtain the pressure increase in a cell. The mass of the pore fluid in an impermeable cell remains the same after a small amount of porosity reduction

$$\varrho_{f,0}\left(1 + \beta p_f^{(1)}\right) V_F^{(1)} = \varrho_{f,0}\left(1 + \beta p_f^{(2)}\right) V_F^{(2)}, \tag{5}$$

where β is the fluid compressibility, $\varrho_{f,0}$ is the fluid density at zero pressure, V_F is the pore volume of the cell and p_f is the pore fluid pressure. The superscripts (1) and (2) denote two consecutive time steps. The fluid density is linear in the fluid pressure where the compressibility is given as

$$\beta = \frac{1}{\varrho_{f,0}} \frac{\Delta\varrho_f}{\Delta p_f}. \tag{6}$$

for simplicity, the compressibilities of the pore space and the solid are assumed to be negligible compared to the compressibility of the fluid, which is taken to be $4 \cdot 10^{-10}$ Pa^{-1}. The mass balance (5) gives that the pressure at the new time step is

$$p_f^{(2)} = p_f^{(1)} \frac{V_F^{(1)}}{V_F^{(2)}} + \frac{1}{\beta} \frac{(V_F^{(1)} - V_F^{(2)})}{V_F^{(2)}}, \tag{7}$$

where the first term is the pressure at the old time step and the second term is the pressure build-up due to compressibility. The first term has a small adjustment necessary to assure mass conservation. The net thickness of a cell is $\Delta\zeta$ and the real thickness of the cell is $h = \Delta\zeta/(1 - \varphi)$, where φ is the porosity. The volume of a cell with base area A is $V = h\, A$ and the pore volume is

$$V_F = \varphi V = e\, A\, \Delta\zeta. \tag{8}$$

arelative change in the pore volume is the same as a relative change in the void ratio

$$\frac{\Delta V_F}{V_F} = \frac{\Delta e}{e}, \tag{9}$$

when the net amount of rock in the cell, $\Delta\zeta$, is constant. Therefore, equation (7) for updating the fluid pressure can be written in terms of the void ratios as

$$p_f^{(2)} = p_f^{(1)} \frac{e^{(1)}}{e^{(2)}} + \frac{1}{\beta} \frac{(e^{(1)} - e^{(2)})}{e^{(2)}}. \tag{10}$$

At each time step, an incremental thickness $\Delta\zeta_T$ of sediment is added uniformly over the seabed, which leads to a decreasing void ratio $\Delta e = e^{(2)} - e^{(1)} = -e_0 \Delta\zeta_T/\zeta_D$, and thereby to the pressure increase of equation (10). The fluid pressure in equations (7) and (10) can also be expressed in terms of the overpressure using the fact that the fluid pressure (p_f) is overpressure (p) plus hydrostatic pressure (p_H), $p_f = p_H + p$.

Equations (1) and (9) show that if the cells had a random surface void ratio e_0, but the same compaction length, then all the cells would have had the same pressure build-up. That is why a random compaction length produces random pressure build-up in the cells, but not a random surface void ratio.

5. Local microfracturing and pressure equilibration

A cell fractures when its fluid pressure reaches the limiting pressure. Fracturing implies that it exchanges fluid with its nearest neighbours. The result of the exchange processes is that the five cells (the cell that fractured and its four nearest neighbours) get the average overpressure of the five cells. It is assumed that the critical fluid pressure opens a microfracture network that allows fluid exchange driven by over-

pressure differences. The overpressure is a fluid flow potential when the fluid density is taken to be constant in Darcy's law. The fluid exchange between a fractured cell and its neighbours is mass conservative. Mass conservation is expressed as

$$\sum_{i\in N} V_{F,i}\,\varrho_{f,0}\cdot\left(1+\beta\cdot(p_{H,i}+p_i)\right)=\sum_{i\in N} V_{F,i}\,\varrho_{f,0}\cdot\left(1+\beta\cdot(p_{H,i}+\bar{p})\right), \tag{11}$$

in terms of the average fluid overpressure $\bar{p}$, which becomes

$$\bar{p}=\frac{\sum_{i\in N} V_{F,i}p_i}{\sum_{i\in N} V_{F,i}} \tag{12}$$

where i is a cell number and N is the set of cells involved in the fracture event. The pore volumes $V_{F,i}$ of each cell do not have the same size because of the random compaction length. Note that the hydrostatic pressure, and therefore the gravity, drops out of the expression for the average overpressure.

After a critical cell has fractured and exchanged its excess fluid with its nearest neighbours, one or more of the nearest neighbour cells might also become critical, and the expulsion process continues. Otherwise, the process has come to an end. If a cell next to the horizontal boundaries fractures, it does not exchange fluid with its neighbours, but expels its excess fluid across the open boundary. The expulsion is done by assigning zero overpressure to the boundary cell. The mass of fluid corresponding to the overpressure drop to zero is accounted for as expelled mass. The total expelled mass at time step n is denoted $M_{\text{exp}}^{(n)}$. The global mass balance of pore fluid is used to check that the expulsion algorithm is mass conservative. The mass balance dictates that the mass of expelled fluid added to the current mass of pore fluid must be equal to the initial mass of pore fluid, which is expressed as

$$\sum_{i\in N_A} V_{F,i}^{(n)}\,\varrho_{f,0}\cdot\left(1+\beta\cdot(p_{H,i}^{(n)}+p_i^{(n)})\right)+M_{\text{exp}}^{(n)}=\sum_{i\in N_A} V_{F,i}^{(0)}\,\varrho_{f,0}\cdot\left(1+\beta\cdot(p_{H,i}^{(0)}+p_i^{(0)})\right), \tag{13}$$

where N_A are all cells in the shale layer. The overpressure and the hydrostatic pressure at step (n) in cell i are denoted by $p_i^{(n)}$ and $p_{H,i}^{(n)}$, respectively. It is of interest to know the total volume of fluid expelled during each step, and is computed using the constant reference fluid density as $V_{\text{exp}}=M_{\text{exp}}/\varrho_{f,0}$. The total expelled mass is comprised of two parts – the total expelled mass downwards and upwards. It should be mentioned that if a cell next to the vertical boundaries fractures, it exchanges fluid with only three nearest neighbours because the vertical boundaries are closed.

6. Demonstration of the expulsion model

This section demonstrates the expulsion model on a shale layer in the interval from $\zeta_1=0$ m to $\zeta_2=1000$ m, which is a depth interval from $z=-3469$ m to $z=-2354$ m. The seabed is initially at $\zeta_T=3000$ m (z = 0 m) and the layer is discretized with 50 × 50 cells. The porosity of the shale layer is shown in Fig. 2a. Expulsion will be studied during the deposition of a small thickness of net sediments, which makes the initial and the final porosity nearly the same. The porosity is produced by the parameters $\varphi_0=0.15(e_0=0.176)$ and a compaction length ζ_c uniformly distributed in the range from 5000 m to 10 000 m, which gives $\zeta_{c,0}=5000$ m and $\Delta\zeta_c=5000$ m in equation (2). The overburden in the layer is taken to be $p_b=\varrho_b g z$, where the bulk density is $\varrho_b=2200$ kgm^{-3} and the gravitational acceleration is $g=9.8$ ms^{-2}. The water depth is considered negligible. The least compressive stress is horizontal and it is 82% of the overburden.

The permeability must be below an upper limit for Darcy flow to be insufficient to expel the excess fluid produced by compaction, and for the cells to be considered impermeable. The upper limit on the permeability can be estimated using the 1-D vertical Darcy flux during compaction (see Appendix A),

$$v_D=\omega\cdot(e-e_{\text{bot}}) \tag{14}$$

where ω is the burial rate and e_{bot} is the void ratio at the base of the layer. The overburden corresponds to an overpressure gradient $dp/dz=\Delta\varrho\, g/(1+e)$, where $\Delta\varrho=\varrho_s-\varrho_f$ is the difference between the grain density and the fluid density. A combination of the Darcy flux (14) with dp/dz as a maximum overpressure gradient gives that an insufficient permeability k is expressed by the condition

$$v_D=\omega\cdot(e-e_{\text{bot}})\gg\frac{k\Delta\varrho g}{(1+e)\mu}. \tag{15}$$

condition (15) gives the upper limit on the permeability as

$$k\ll k_{\max}=(1+e)\,e_0\frac{(\zeta_2-\zeta_1)}{\zeta_D}\frac{\mu\omega}{\Delta\varrho g} \tag{16}$$

where the average linear void ratio (3) is used in the second equality. The pressure gradient $\Delta\varrho g=1.03\cdot10^4$ Pa/m, the viscosity $\mu=1\cdot10^{-3}$ Pa s, the burial rate $\omega=100$ m Ma^{-1}, the layer thickness $\zeta_2-\zeta_1=1000$ m, the surface void ratio $e_0=0.15$, the void ratio $e=0.1$, and the compaction length $\zeta_D=5000$ m give that $k_{\max}=1\cdot10^{-20}$ m^2. For example, during periods with an order of magnitude larger burial rates, the upper limit on the permeability, $k_{\max}$, is one order of magnitude larger. Permeabilities of this order and lower are measured in shales (Yang and Aplin, 2007; Mondol et al., 2008; Neuzil, 2019). The limiting permeability $k_{\max}$ in equation (16) can be interpreted as a fracture permeability, see Wangen (2010). It is the permeability that gives the expulsion from the compaction process when the fluid pressure corresponds to the overburden.

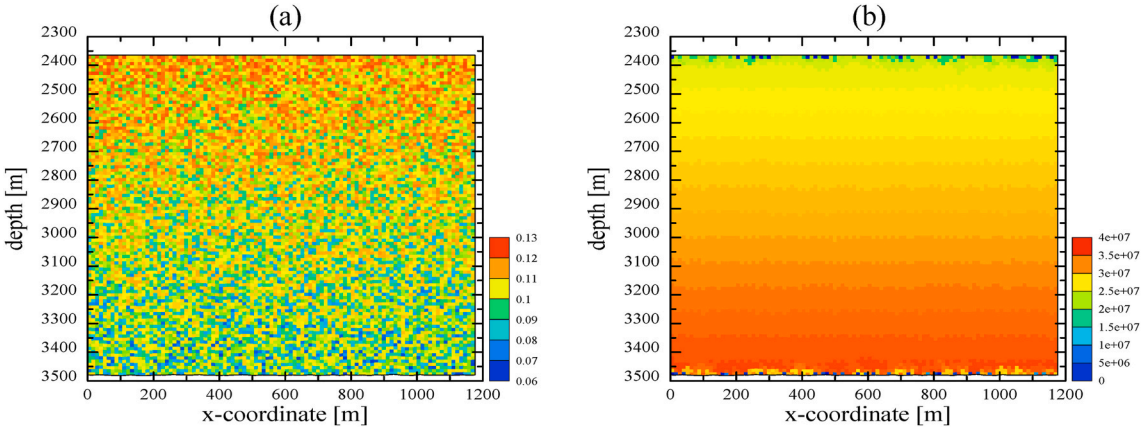

Fig. 2. (a) The porosity, [-]. (b) The final overpressure, [Pa]. The depth interval is from z = 3469 m ($\zeta_1=0$ m) to z = 2354 m ($\zeta_2=1000$ m) in both figures.

The initial pressure build-up is skipped in the model, where the pore pressure goes from hydrostatic to critical. Instead, the pore pressure is initialized with 99% of the fracture pressure. Then, fluid expulsion is studied during the addition of a total of 1 m of sediments to the surface, where the total is divided into 50 deposition steps of 0.02 m. Each deposition step creates overpressure that drives expulsion by micro-fracturing. It is not necessary to specify the duration of each step, as long it is sufficiently short for the permeability to be much less than the maximum permeability estimated equation (16). The example above shows that a deposition rate of at least $\omega = 100$ m Ma^{-1} is needed when the layer permeability is as low as $1 \cdot 10^{-20}$ m^2.

Fig. 2b shows the overpressure at the end of a typical deposition step, when the expulsion algorithm has brought the pressure in each cell below the critical level.

Fig. 3a shows the critical cells produced by the addition of $\Delta\zeta_T$ with a white colour for the same simulation as shown in Fig. 2. These critical cells are fractured in turn, and they share excess fluid with their nearest neighbours. Their nearest neighbour cells may become critical, which again leads to the further spread of the initial excess fluid. Excess fluid may be passed back and forth between the cells several times until no more cells are critical.

The colour scale in Fig. 3a shows how many times a cell is involved in an equilibration process. It shows that the cells are increasingly involved with equilibration towards the surface. The reason is that the compressive stress decreases with decreasing depth. When fluid is passed to the neighbour cells, the cell above a fractured cell is more likely to become critical than the cell below. The result is a net movement of the fluid upwards.

Fig. 3b shows all cells involved in equilibration during a deposition step as connected clusters for the same simulation as in Fig. 3a. The cells between the clusters were never critical during the step. These clusters are dependent on the step size $\Delta\zeta_T$. A large $\Delta\zeta_T$ implies that a large number of cells are critical and that nearly all cells are involved in an equilibration process, and that they belong to the same cluster. In the other limit with very small steps $\Delta\zeta_T$, there may be deposition steps where no cells or very few cells are critical.

7. Expulsion rate

The total expulsion per deposition step from the layer is intermittent, and depends on the grid size, as seen in Fig. 4. The variation in expelled volumes approaches the average with decreasing cell size and the model approaches a continuum model in the limit of zero cell size. This behaviour of the model is insensitive to the deposition size $\Delta\zeta_T$, which is driving the expulsion process.

It is straightforward to estimate the volume of expelled fluid based on the averaged void ratio for the entire layer $\overline{\overline{e}}$, given by function (1). The total pore volume of the layer is

$$V_{\varphi,\mathrm{tot}}(\zeta_T) = \overline{\overline{e}}(\zeta_T)\, V_{\zeta,\mathrm{tot}}, \tag{17}$$

where $V_{\zeta,\mathrm{tot}}$ is the net (porosity free) volume of sediments in the shale layer. The total amount of porosity free sediment in the shale unit rests constant during compaction. Therefore, the pore volume depends only on the average void ratio, which again is a function of the basin thickness ζ_T. The total volume of expelled fluid is the difference between the initial pore volume and the current pore volume

$$V_{\mathrm{exp}} \approx \left(\overline{\overline{e}}(\zeta_T^{(0)}) - \overline{\overline{e}}(\zeta_T^{(n)})\right)\cdot V_{\zeta,\mathrm{tot}} \tag{18}$$

$$= e_0 \cdot V_{\zeta,\mathrm{tot}} \cdot \left(\zeta_T^{(n)} - \zeta_T^{(0)}\right) \Big/ \zeta_D, \tag{19}$$

where $\zeta_T^{(0)}$ and $\zeta_T^{(n)}$ are the initial and the current net thicknesses of the basin, respectively. The volume of expelled fluid is proportional to the sediment thickness deposited in the time interval, $\zeta_T^{(n)} - \zeta_T^{(0)}$. Fig. 5 shows the numerically computed volume of expelled fluid and the volume estimate (19), and the match is good. A volume estimate of expulsion per deposition step is simply V_{exp} of equation (19) divided by the number n of steps

$$\Delta V_{\mathrm{exp}} \approx e_0 \cdot V_{\zeta,\mathrm{tot}} \cdot \Delta\zeta_T / \zeta_D. \tag{20}$$

using the case data $e_0 = 0.176$ (from $\varphi_0 = 0.15$), $V_{\zeta,\mathrm{tot}} = 1.176 \cdot 10^6$ m^3, $\zeta_D = 7214$ m and $\Delta\zeta_T = 0.02$ m gives the average expulsion per time step as $\Delta V_{\mathrm{exp}} = 0.58$ m^3/step, which is in excellent agreement with the averages in Fig. 4. The expelled volume per deposition step becomes the expulsion rate when divided by the duration of the deposition step. For example, a net deposition rate $\omega = 1$ m Ma^{-1} gives an expulsion rate of $dV_{\mathrm{exp}}/dt = 32.5$m^{3}Ma from the layer.

The numerical model measures expulsion across the upper horizontal boundary and the lower horizontal boundary. In this case, 94% of expelled fluid was across the upper horizontal boundary and the remaining 6% was across the lower horizontal boundary. The other cases have a similar distribution of flow across the horizontal boundaries.

8. Random cell strength

The heterogeneous nature of rocks affects the porosity and also the strength. The previous cases have expulsion from a shale layer where the limiting fluid pressure is a strictly increasing function of depth. The addition of random strength to each cell can make the limiting pressure

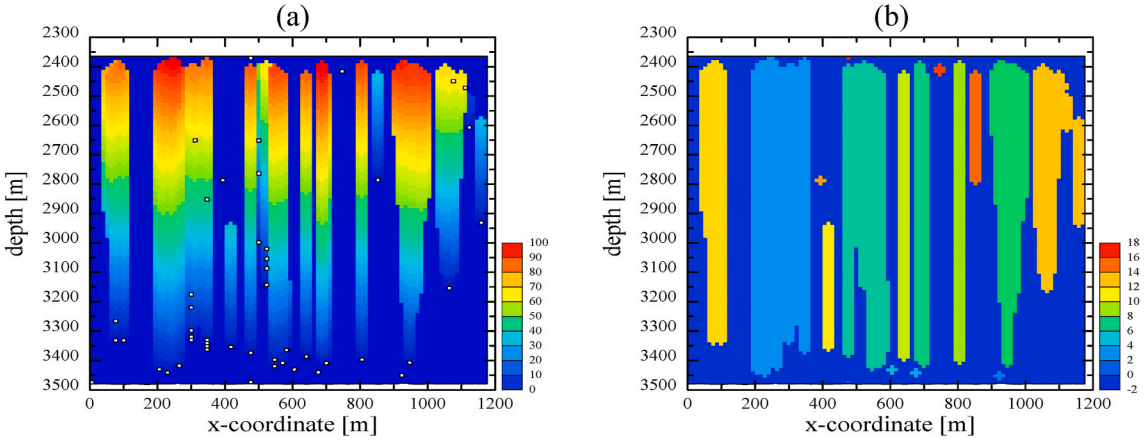

Fig. 3. (a) The initial critical cells are shown with white colour. The colour scale shows the number of times the cells were involved in pore pressure equilibration. (b) The clusters of cells involved in pressure equilibration. The colour scale shows the enumeration of the clusters.

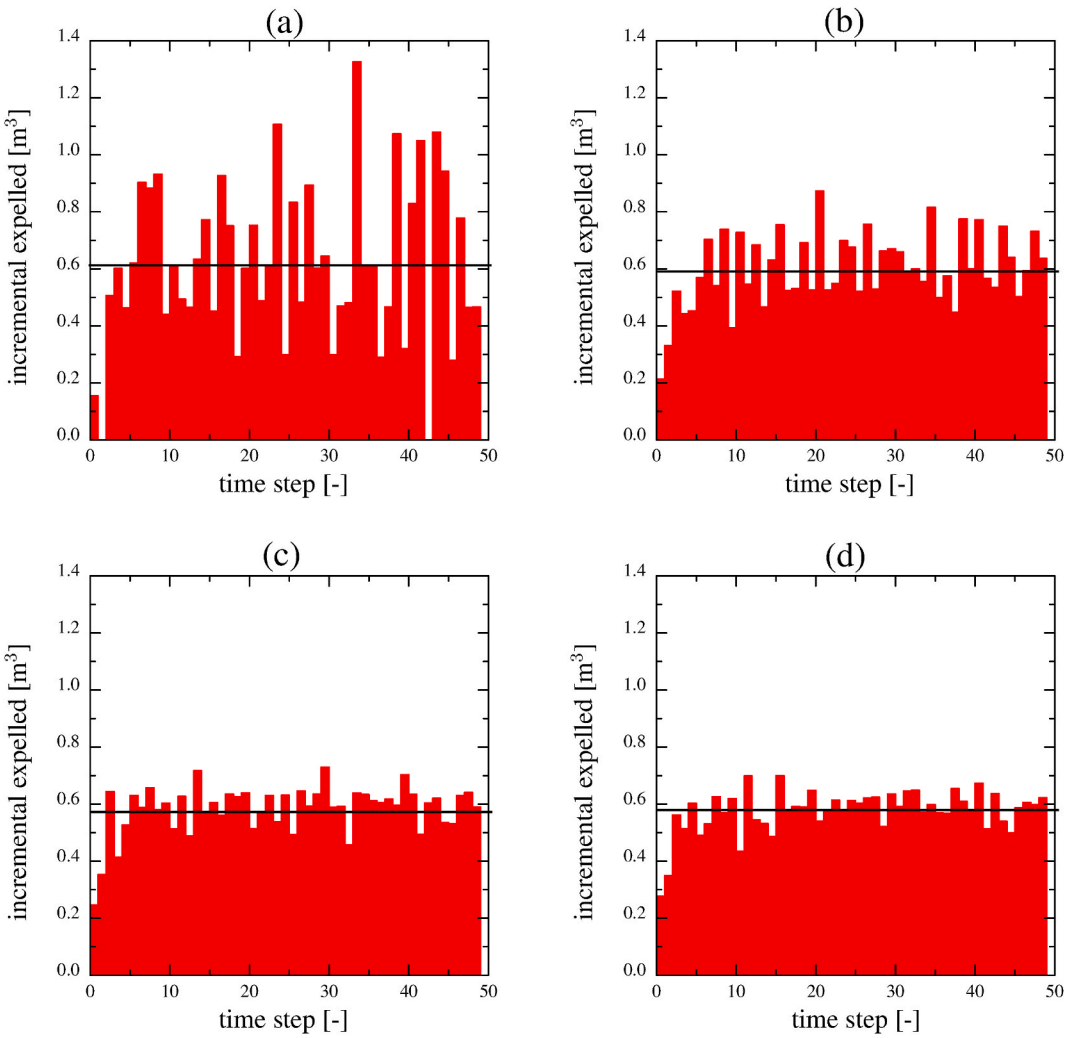

Fig. 4. The expelled volume at each depositional increment from step 0 to step 50. The black horizontal line is the average over the time steps. (a) 100x100-cells-grid. (b) 200x200-cells-grid. (c) 300x300-cells-grid. (d) 400x400-cells-grid.

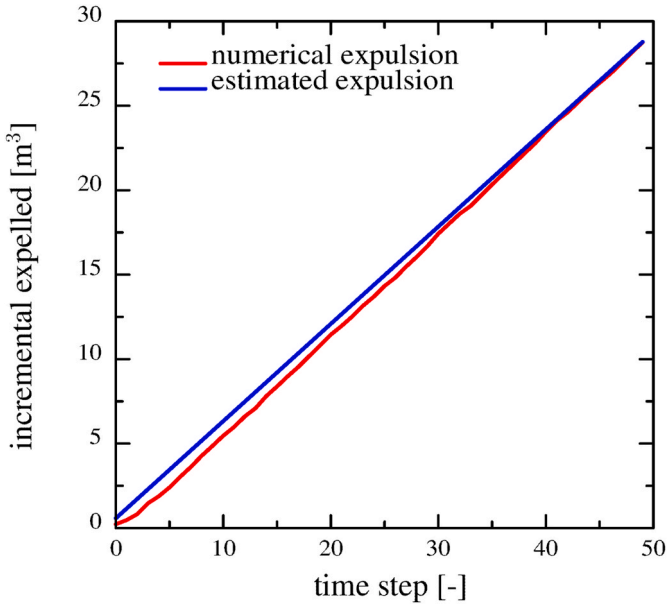

Fig. 5. The total expelled volume from the shale layer in Fig. 4a, where a 100 × 100 cells grid was used. The exulsion is estimated with equation (19).

locally decreasing with depth at a large number of places.

When the critical pressure includes random strength, the pressure equilibration algorithm will not be able to remove all critical cells. A cell may remain critical after an equilibration step if the cell and its neighbours already have the same overpressure from the previous equilibration process. A new equilibration process will then just reproduce the same average pressure for the critical cell and its neighbours. In the same way, it is also possible for a cluster of critical cells to remain critical after an equilibration process. Fig. 6 shows an example with random strength, where the strength of 1 MPa is uniformly distributed on the cells. All remaining critical cells are shown as white in Fig. 6b. The pattern of white cells will be reproduced by a new equilibration iteration and, therefore, they cannot be removed. The coloured legend in Fig. 6 shows how many times a cell has been involved in pressure equilibration, and demonstrates that remaining critical cells and their neighbours are involved in a large number of equilibration steps before the pattern of critical cells becomes stationary. Despite the random rock strength, 97.5% of the migration is upwards and only 2.5% is downwards. Migration downwards could be a boundary effect when cells along the lower boundary become critical.

The critical clusters have cells with a pressure that is beyond the least compressive stress, and these cells could represent pockets of fluid stored in open fracture networks. The size distribution of the clusters is shown in Fig. 7. Fig. 7 shows the number of clusters N larger than a cluster size S, where the size is given by the number of cells in the

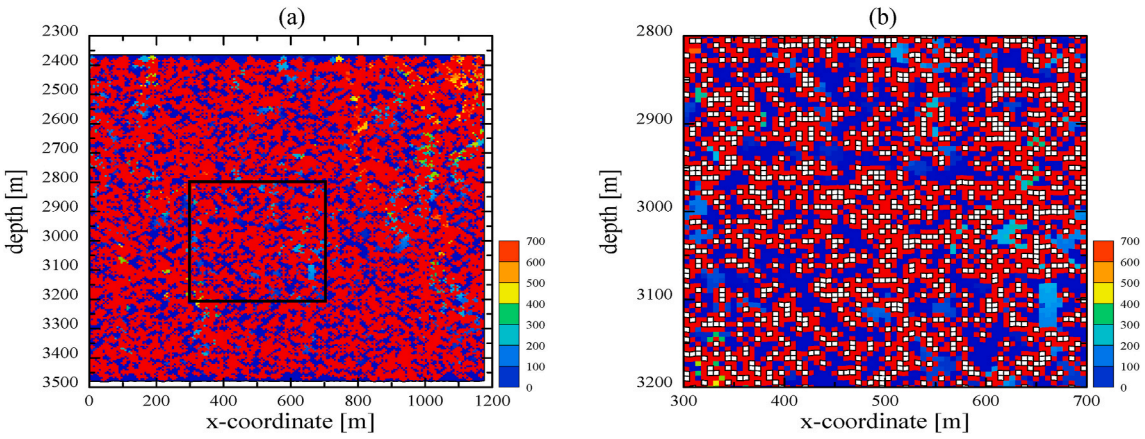

Fig. 6. The colours show how many times a cell was involved in an equilibration step. (b) A zoom-in on the rectangle in figure (a) where the cells that remain overpressured are shown as white. The depth interval is from z = 3469 m ($\zeta_1 = 0$ m) to z = 2354 m ($\zeta_2 = 1000$ m).

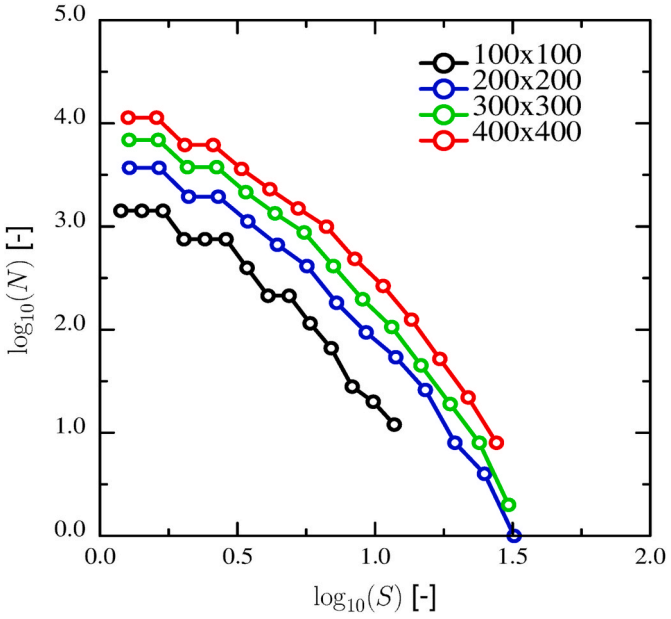

Fig. 7. The number of clusters N larger than cluster size S is plotted as a function of S.

cluster. Further simulations are needed to fit a linear slope to the size-frequency distribution of the critically pressurized clusters.

The author is not aware of any direct evidence for such over-pressured pockets of fracture fluid. A possible indication of pockets with open fractures are cemented fracture networks (Anders et al., 2014). The minerals that precipitate inside the fracture could be due to a higher equilibrium concentration in the host rock than in the fractures (Wangen and Munz, 2004). Fracture cementation requires that the pockets are open sufficiently long for cementation to be noticeable. The thickness of the cement indicates how long time the fracture network was open for mineral precipitation.

9. Discussion

Fluid pressure in sedimentary basins is often divided into three depth intervals, where the first interval from the seabed and downwards has near hydrostatic conditions. The second interval is a transition zone where the fluid pressure increases from hydrostatic to near lithostatic conditions, and the third interval is a nearly lithostatic continuation underneath the transition zone (Leftwich and Engelder, 1994; Nadeau, 2011; Goulty et al., 2012; Zhao et al., 2018; Riis and Wolff, 2020). The transition zone spans the temperature range from 70 °C to 120 °C, and it corresponds to the onset of diagenesis and hydrocarbon generation (Nadeau, 2011). Above the transition zone, the porosity loss is by mechanical compaction controlled by the effective fluid pressure. Through the transition zone, mechanical compaction becomes replaced by chemical compaction controlled by temperature. HPHT is the term that denotes the high-pressure and high-temperature conditions underneath the transition zone. Several geochemical processes reduce the porosity and the permeability of shales, such as precipitation of microquartz (Thyberg et al., 2009; Thyberg and Jahren, 2011). The chemical compaction process makes the shales almost impermeable. This pattern of three depth intervals of fluid pressure has been observed in sedimentary basins worldwide (Nadeau, 2011).

Fluid expulsion in depth intervals of HPHT is not likely to be by Darcy flow, since the HPHT pressure conditions are at the fluid fracture pressure. Furthermore, there does not appear to be any feedback from the fluid pressure that stops the chemical compaction processes when the fluid pressure approaches the lithostatic pressure (Wangen, 2001). For this reason, chemical compaction models based on Darcy flow can produce overpressure that exceeds the lithostatic pressure with a large margin in the HPHT depth interval (Wangen, 1997, 2001).

When applied to fluid expulsion in tight sedimentary rocks, the TS algorithm has a fluid pressure given by the least compressive stress, which often is close to the lithostatic stress. Therefore, the TS algorithm is a simple and a robust model for fluid expulsion of tight sedimentary rocks, which operates at fluid fracture pressures observed in the HPHT depth intervals. At the same time, the TS algorithm expels excess fluid from the compaction process in a mass conservative manner. Expulsion is in the direction of decreasing least compressive stress, which is also the direction of decreasing overpressure.

The TS algorithm has been applied to model expulsion of brine from tight shales, but it could equally well have been used as a basis for modelling expulsion of hydrocarbons. Another possible application of the TS algorithm is the modelling of pipe structures in sedimentary basins. These structures are mapped by seismic imaging, and they are interpreted as blow-out structures resulting from overpressured aquifers and reservoirs (Løseth et al., 2009; Kartens et al., 2017). The proposed model can be extended with time-dependent healing of fractures. Time dependence can also, be introduced by a non-constant deposition rate.

10. Conclusion

Pore fluid pressure in sedimentary basins is rarely observed above the overburden pressure. It appears that natural hydraulic fracturing is the process that limits pressure build-up to the least compressive stress.

The "Toggle Switch" (TS) model of Miller and Nur (2000) was tested as an algorithm for the expulsion of brine by hydraulic fracturing in an impermeable layer that undergoes burial and compaction. The impermeable layer is represented by a regular grid of cells, where each cell has local pressure build-up. Deposition of sediments drives the pressure build-up. The deposition process is represented by small steps, where each step leads to a small loss of porosity and a corresponding small pressure increase.

The cells are assigned a void ratio that decreases linearly with depth, where depth is measured from the surface as net (porosity free) rock. It is a linear approximation of a void ratio trend in the layer during a short time interval of burial and compaction. Furthermore, the void ratio is random by means of a random compaction length in each cell, which implies random local pressure build-up by compaction. Since the void ratio is linear by depth, it is straightforward to compute the layer average of the random void ratio and the total pore volume of the layer. The expression for the total pore volume is used to approximate the fluid expulsion rate, and to estimate an effective permeability for the hydrofractured sediments.

The TS algorithm was applied at each deposition step to redistribute pore fluid away from critically pressured cells. A cell becomes critical when the pore pressure exceeds the least compressive stress, which is taken to be close to the overburden pressure. Simulations show that the fluid is expelled upwards because the least compressive stress is decreasing upwards. The total amount of fluid expelled from the layer per step depends on the grid size and the random porosity, and approaches a constant average value with decreasing cell size.

When the least compressive stress is strictly decreasing with decreasing depth, the TS algorithm makes all critical cells non-critical. The cells can be assigned random strength, which implies that the least compressive stress is locally non-decreasing towards the surface. With random strength, clusters of critically pressured cells may remain that the TS algorithm cannot remove. These clusters appear to have a logarithmic size-frequency distribution. An overpressured cluster could represent an open and connected fracture network. The TS algorithm produces expulsion upwards regardless of random strength, as long as the global trend of the least compressive stress is decreasing with depth. Then, redistribution of fluid from a critical cell or a cluster of critical cells by the TS algorithm is more likely to make a cell above the cluster critical than a cell below the cluster.

It is concluded that the TS algorithm is a well-adapted model for the expulsion of fluids from a tight compacting sedimentary layer. The TS algorithm limits the pressure build-up in the layer to the least compressive stress. The results of the TS algorithm, rather than the algorithm itself, can be implemented in basin simulators. It is done by first computing the overpressure and the corresponding Darcy flux. Then, for cells where the fluid pressure exceeds the fracture pressure, the fluid pressure is simply assigned the value of the fracture pressure. The effective fracture permeability for a cell is estimated by combining the expression for the Darcy flux with the vertical gradient of the fracture pressure. The TS algorithm can also be used as a basis for other fracture driven processes in sedimentary basins, such as expulsion of hydrocarbons and chimney formation.

Credit author statement

The author Magnus Wangen is alone responsible for the work presented in the manuscript: That includes the: Conceptualization; Data curation; Formal analysis; Investigation; Methodology; Project administration; Resources; Software; Supervision; Validation; Visualization; Roles/Writing –original draft; Writing – review & editing.

Declaration of competing interest

The authors declare that they have no known competing financial interests or personal relationships that could have appeared to influence the work reported in this paper.

Acknowledgements

Parts of this work were supported by the Research Council of Norway through Project 280 567 "CO2-Paths". The authors are grateful for the suggestions and corrections to the manuscript made by two anonymous reviewers and associate editor Mark Engle.

Appendix A. The vertical Darcy flux

Conservation of mass of pore fluid in the vertical direction is expressed in the ζ-coordinate as

$$\frac{\partial e}{\partial t}+\frac{\partial v_D}{\partial \zeta}=0, \tag{21}$$

where e is the void ratio and v_D is the Darcy flux, see Wangen (2010). Expression (21) assumes that the fluid and solid densities are constant. It is straightforward to integrate equation (21) when the void ratio is functions depth from the sediment surface measured as net (porosity free) rock, $e=e(u)$, where the net depth is $u=\omega t-\zeta$. Deposition takes place at a constant rate ω. Then, mass conservation of the pore fluid, equation (21), gives that

$$v_D(\zeta)=-\int_0^{\zeta}\frac{\partial e}{\partial t}\,d\zeta=-\int_0^{\zeta}\frac{de}{du}\frac{du}{dt}\,d\zeta=\int_{u(0)}^{u(\zeta)}\frac{de}{du}\omega\,du=\omega\cdot(e(\zeta)-e_{\mathrm{bot}}), \tag{22}$$

where e_{bot} is the void ratio at the base of the layer ($\zeta=0$) and it is assumed that $v_D=0$ at $\zeta=0$.

References

Anders, M.H., Laubach, S.E., Scholz, C.H., 2014. Microfractures: a review (and Structures in Fold and Thrust Belts with Recognition of the Work of David V. Wiltschko). J. Struct. Geol. 69, 377–394. https://doi.org/10.1016/j.jsg.2014.05.011,fluids. ISSN 0191-8141.

Appold, M.S., Nunn, J.a., 2002. Numerical models of petroleum migration via buoyancy-driven porosity waves in viscously deformable sediments. Geofluids 2 (3), 233–247. https://doi.org/10.1046/j.1468-8123.2002.00040.x. ISSN 14688115.

Atkinson, J., Bransby, P., 1978. The Mechanics of Soils: an Introduction to Critical State Soil Mechanics. McGraw-Hill Book Co, London; New York, ISBN 0070840792.

Audet, D., Fowler, A., 1992. A mathematical model for compaction in sedimentary basins. Geophys. J. Int. 110 (3), 577–590. https://doi.org/10.1111/j.1365-246X.1992.tb02093.x.

Bethke, C.M., Corbet, T.F., 1988. Linear and nonlinear solutions for one-dimensional compaction flow in sedimentary basins. Water Resour. Res. 24 (3), 461–467. https://doi.org/10.1029/WR024i003p00461.

Bjørlykke, K., 2010. From Sedimentary Environments to Rock Physics. Springer-Verlag, Berlin Heidelberg, p. 508.

Bjørlykke, K., Høeg, K., 1997. Effects of burial diagenesis on stresses, compaction and fluid flow in sedimentary basins. Mar. Petrol. Geol. 14 (3), 267–276. https://doi.org/10.1016/S0264-8172(96)00051-7. ISSN 0264-8172.

Bruel, D., 2007. Using the migration of the induced seismicity as a constraint for fractured Hot Dry Rock reservoir modelling. Int. J. Rock Mech. Min. Sci. 44 (8), 1106–1117. https://doi.org/10.1016/j.ijrmms.2007.07.001. ISSN 1365-1609.
Bruel, D., Charlety, J., 2007. Moment-frequency distribution used as a constraint for hydro-mechanical modelling in fracture networks. In: International Society for Rock Mechanics, 11th ISRM Congress, pp. 1–5. Portugal, Lisbon, Portugal.
Rocks Mechanics Charlez, P., 1997, chap. 6. Petroleum Applications, vol. II. Édition Technip, Paris.
Darby, D., Haszeldine, R., Couples, G., 1998. Basin Modelling, Chap. Central North Sea Overpressures: Insights into Fluid Flow from One- and Two-Dimensional Basin Modelling. Geological Society special publication, Geological Society of London, United Kingdom, ISBN 1862390088, pp. 95–107. https://doi.org/10.1144/GSL.SP.1998.141.01.06.
de Riese, T., Bons, P.D., Gomez-Rivas, E., Sachau, T., 2020. Interaction between crustal-scale Darcy and hydrofracture fluid transport: a numerical study. Geofluids 2020, 1–14. https://doi.org/10.1155/2020/8891801.
Gibson, R.E., 1958. The progress of consolidation in a clay layer increasing in thickness with time. Geotechnique 8 (4), 171–182. https://doi.org/10.1680/geot.1958.8.4.171.
Goulty, N.R., Ramdhan, A.M., Jones, S.J., 2012. Chemical compaction of mudrocks in the presence of overpressure. Petrol. Geosci. 18 (4), 471–479. https://doi.org/10.1144/petgeo2012-018. ISSN 1354-0793.
Hafver, A., Jettestuen, E., Feder, J., Meakin, P., Malthe-Sørenssen, A., 2014. A node-splitting discrete element model for fluid–structure interaction. Phys. Stat. Mech. Appl. 416, 61–79. https://doi.org/10.1016/j.physa.2014.08.039. ISSN 0378-4371.
Hermanrud, C., Undertun, O., 2019. Resolution limits of fluid overpressures from mineralogy, porosity, and sonic velocity variations in North Sea mudrocks. AAPG (Am. Assoc. Pet. Geol.) Bull. 103 (11), 2665–2695. https://doi.org/10.1306/02251917057. ISSN 0149-1423.
Hermanrud, C., Wensaas, L., Teige, G., Bolas, H.N., Hansen, S., Vik, E., 1998. Shale porosities from well logs on Haltenbanken (Offshore Mid-Morway) show no influence of overpressuring. chap. 4 The American Association of Petroleum Geologists 65–85.
Hermanrud, C., Nordgård Bolås, H., Teige, G., 2005. Seal Failure Related to Basin-Scale Processes. chap. 2. AAPG Hedberg Series, pp. 12–22, 2.
Hubbert, M., Willis, D., 1957. Mechanics of hydraulic fracturing. Petroleum Transactions AIME 210, 153–168.
Itasca International, I., 2016. Universal Distinct Element Code (UDEC), Version 6.0. http://www.itascacg.com/software/udec.
Izadi, G., Elsworth, D., 2014. Reservoir stimulation and induced seismicity: Roles of fluid pressure and thermal transients on reactivated fractured networks. Geothermics 51, 368–379. https://doi.org/10.1016/j.geothermics.2014.01.014. ISSN 03756505.
Josh, M., Esteban, L., Delle Piane, C., Sarout, J., Dewhurst, D., Clennell, M., 2012. Laboratory characterisation of shale properties. J. Petrol. Sci. Eng. 88–89, 107–124. https://doi.org/10.1016/j.petrol.2012.01.023. ISSN 0920-4105.
Kartens, J., Ahmed, W., Berndt, C., Class, H., 2017. Focused fluid flow and the sub-seabed storage of CO2: evaluating the leakage potential of seismic chimney structures for the Sleipner CO2 storage operation. Mar. Petrol. Geol. 88, 81–93.
Kobchenko, M., Panahi, H., Renard, F., Dysthe, D.K., Malthe-Sørenssen, A., Mazzini, A., Scheibert, J., Jamtveit, B., Meakin, P., 2011. 4D imaging of fracturing in organic-rich shales during heating. J. Geophys. Res. Solid Earth 116 (B12), 1–9. https://doi.org/10.1029/2011JB008565.
Kobchenko, M., Hafver, A., Jettestuen, E., Renard, F.m. c., Galland, O., Jamtveit, B., Meakin, P., Dysthe, D.K., 2014. Evolution of a fracture network in an elastic medium with internal fluid generation and expulsion. Phys. Rev. E 90, 052801. https://doi.org/10.1103/PhysRevE.90.052801.
Lee, E.Y., Novotny, J., Wagreich, M., 2020. Compaction trend estimation and applications to sedimentary basin reconstruction (BasinVis 2.0). Applied Computing and Geosciences 5, 100015. https://doi.org/10.1016/j.acags.2019.100015. ISSN 2590–1974.
Leftwich, J., John, T., Engelder, T., 1994. The characteristics of geopressure profiles in the gulf of Mexico basin. In: Basin Compartments and Seals. American Association of Petroleum Geologists, ISBN 9781629810935, pp. 119–129. https://doi.org/10.1306/M61588C8.
Løseth, H., Gading, M., Wensaas, L., 2009. Hydrocarbon leakage interpreted on seismic data. Mar. Petrol. Geol. 26 (7), 1304–1319. https://doi.org/10.1016/j.marpetgeo.2008.09.008. ISSN 02648172.
Miller, S., Nur, A., 2000. Permeability as a toggle switch in fluid-controlled crustal processes. Earth Planet Sci. Lett. 183 (1–2), 133–146. https://doi.org/10.1016/S0012-821X(00)00263-6. ISSN 0012821X.
Mondol, N.H., Bjørlykke, K., Jahren, J., 2008. Experimental compaction of clays: relationship between permeability and petrophysical properties in mudstones. Petrol. Geosci. 14 (4), 319–337. https://doi.org/10.1144/1354-079308-773. ISSN 1354-0793.
Nadeau, P.H., 2011. Earth's energy "Golden Zone": a synthesis from mineralogical research. Clay Miner. 46 (1), 1–24. https://doi.org/10.1180/claymin.2011.046.1.1. ISSN 0009-8558.
Neuzil, C., 2019. Permeability of clays and shales. Annu. Rev. Earth Planet Sci. 47 (1), 247–273. https://doi.org/10.1146/annurev-earth-053018-060437.
Nordgård Bolås, H.M., Hermanrud, C., Teige, G.M.G., 2004. Origin of overpressures in shales: constraints from basin modeling. AAPG (Am. Assoc. Pet. Geol.) Bull. 88 (2), 193–211. https://doi.org/10.1306/10060302042. ISSN 0149-1423.
Nordgren, R., 1972. Propagation of a vertical hydraulic fracture. Society of Petroleum Engineers Journal SPE 3009, 306–314.
Osborne, M.J., Swarbrick, R.E., 1997. Mechanisms for generating overpressure in sedimentary basins: a reevaluation. AAPG (Am. Assoc. Pet. Geol.) Bull. 81 (6), 1023–1041.
Panahi, H., Kobchenko, M., Meakin, P., Dysthe, D.K., Renard, F., 2019. Fluid expulsion and microfracturing during the pyrolysis of an organic rich shale. Fuel 235, 1–16. https://doi.org/10.1016/j.fuel.2018.07.069. ISSN 0016-2361.
Perkins, K., Kern, L., 1961. Widths of hydraulic fractures. J. Petrol. Technol. 13, 937–949.
Riahi, A., Damjanac, B., 2013. Numerical study of hydro-shearing in geothermal reservoirs with a pre-existing discrete fracture network. In: Proceedings, Thirty-Eighth Workshop on Geothermal Reservoir Engineering. Stanford University, California, pp. 1–13.
F. Riis, A. Wolff, Use of Pore Pressure Data from the Norwegian Continental Shelf to Characterize Fluid-Flow Processes in Geological Timescales, Geological Society, London, Special Publications vol. 495, ISSN 0305-8719, doi:10.1144/SP495-2018-176.
Sachau, T., Bons, P., Gomez-Rivas, E., 2015. Transport efficiency and dynamics of hydraulic fracture networks. Frontiers in Physics 3, 1–13. https://doi.org/10.3389/fphy.2015.00063. ISSN 2296-424X.
Teige, G., Hermanrud, C., Wensaas, L., Bolås, H.N., 1999. The lack of relationship between overpressure and porosity in North Sea and Haltenbanken shales. Mar. Petrol. Geol. 16 (4), 321–335. https://doi.org/10.1016/S0264-8172(98)00035-X. ISSN 0264-8172.
Thyberg, B., Jahren, J., 2011. Quartz cementation in mudstones: sheet-like quartz cement from clay mineral reactions during burial. Petrol. Geosci. 17 (1), 53–63. https://doi.org/10.1144/1354-079310-028. ISSN 1354-0793.
Thyberg, B., Jahren, J., Winje, T., Bjørlykke, K., Faleide, J., 2009. From mud to shale: rock stiffening by micro-quartz cementation. First Break 27 (2). https://doi.org/10.3997/1365-2397.2009003. ISSN 1365-2397, URL. https://www.earthdoc.org/content/journals/10.3997/1365-2397.2009003.
Tremosa, J., Gailhanou, H., Chiaberge, C., Castilla, R., Gaucher, E.C., Lassin, A., Gout, C., Fialips, C., Claret, F., 2020. Effects of smectite dehydration and illitisation on overpressures in sedimentary basins: a coupled chemical and thermo-hydro-mechanical modelling approach. Mar. Petrol. Geol. 111, 166–178. https://doi.org/10.1016/j.marpetgeo.2019.08.021. ISSN 0264-8172.
Tzschichholz, F., Herrmann, H., 1995. Simulations of pressure fluctuations and acoustic emission in hydraulic fracturing. Phys. Rev. E 51, 1961–1970.
Tzschichholz, F., Wangen, M., 1998. Modelling of Hydraulic Fracturing of Porous Materials. chap. 8. WIT Press, Southhampton, pp. 227–260.
Tzschichholz, F., Herrmann, H., Roman, H., Pfuff, M., 1994. Beam model for hydraulic fracturing. Phys. Rev. B 49, 7056–7059.
Verdon, J.P., Stork, A.L., Bissell, R.C., Bond, C.E., Werner, M.J., 2015. Simulation of seismic events induced by CO2 injection at in Salah, Algeria. Earth Planet Sci. Lett. 426, 118–129. https://doi.org/10.1016/j.epsl.2015.06.029. ISSN 0012821X.
Walderhaug, O., Bjørkum, P.A., Nadeau, P.H., Langnes, O., 2001. Quantitative modelling of basin subsidence caused by temperature-driven silica dissolution and reprecipitation. Petrol. Geosci. 7 (2), 107–113. https://doi.org/10.1144/petgeo.7.2.107. ISSN 1354-0793.
Wangen, M., 1992. Pressure and temperature evolution in sedimentary basins. Geophysics Journal International 110, 601–613.
Wangen, M., 1997. A simple model of pressure build-up caused by porosity reduction during burial. Geophys. J. Int. 130, 757–764.
Wangen, M., 2001. A quantitative comparison of some mechanisms generating overpressure in sedimentary basins. Tectonophysics 334, 211–234.
Wangen, M., 2010. Physical Principles of Sedimentary Basin Analysis. Cambridge University Press.
Wangen, M., 2011. Finite element modelling of hydraulic fracturing on a reservoir scale in 2D. J. Petrol. Sci. Eng. 77, 274–285. https://doi.org/10.1016/j.petrol.2011.04.001.
Wangen, M., 2019. A 3D model of hydraulic fracturing and microseismicity in anisotropic stress fields. Geomechanics and Geophysics for Geo-Energy and Geo-Resources 5 (1), 17–35. https://doi.org/10.1007/s40948-018-0096-4.
Wangen, M., Munz, I.A., 2004. Formation of quartz veins by local dissolution and transport of silica. Chem. Geol. 209 (3), 179–192. https://doi.org/10.1016/j.chemgeo.2004.02.011. ISSN 0009-2541.
Whitlow, R., 2001. Basic Soil Mechanics. Pearson Education Ltd, Prentice Hall, England, p. 571.
Y. Yang, A. C. Aplin, Permeability and petrophysical properties of 30 natural mudstones, J. Geophys. Res. Solid Earth 112 (B3), doi:https://doi.org/10.1029/2005JB004243.
Yardley, G., Nwozor, K., 2017. Overpressure Mechanisms and Their Distribution in the Central North Sea. European Association of Geoscientists and Engineers, pp. 2214–4609. https://doi.org/10.3997/2214-4609.201700048.
Yarushina, V.M., Podladchikov, Y.Y., 2015. (De)compaction of porous viscoelastoplastic media: model formulation. J. Geophys. Res. Solid Earth 120 (6), 4146–4170. https://doi.org/10.1002/2014JB011258.
Yarushina, V.M., Podladchikov, Y.Y., Connolly, J.A.D., 2015. (De)compaction of porous viscoelastoplastic media: solitary porosity waves. J. Geophys. Res. Solid Earth 120 (7), 4843–4862. https://doi.org/10.1002/2014JB011260.
Zhang, L., Nasika, C., Donzé, F.-V., Zheng, X., Renard, F., Scholtès, L., 2019. Modeling porosity evolution throughout reaction-induced fracturing in rocks with implications for serpentinization. J. Geophys. Res. Solid Earth 124 (6), 5708–5733. https://doi.org/10.1029/2018JB016872.
Zhao, J., Li, J., Xu, Z., 2018. Advances in the origin of overpressures in sedimentary basins. Petroleum Research 3 (1), 1–24. https://doi.org/10.1016/j.ptlrs.2018.03.007. ISSN 2096-2495.